Results in Optics 21 (2025) 100858

Contents lists available at ScienceDirect

Results in Optics

journal homepage: www.sciencedirect.com/journal/results-in-optics

# Power optimization of 1:2 and 1:4 photonic crystal based optical power splitters/combiners using machine learning algorithms

Kalyan Kumar Ghosh [a], Haraprasad Mondal [a,*], Himanshu Ranjan Das [b], Mohammad Soroosh [c], Sudipta Majumder [a], Bhargabjyoti Saikia [a]

[a] Dibrugarh University Institute of Engineering and Technology, Dibrugarh University, Assam, India
[b] Department of Electronics and Communication Engineering, School of Engineering, Central University of Karnataka, Kalaburagi, Karnataka 585367, India
[c] Department of Electrical Engineering, Shahid Chamran University of Ahvaz, Ahvaz, Iran

ARTICLE INFO

*Keywords:*
Optical waveguides
Power splitter
Fiber optic networks
Machine learning algorithm
Finite difference time domain

ABSTRACT

Optical power splitters play a vital role in signal distribution, network expansion, and both balanced and unbalanced power splitting in cost-efficient fiber optic systems. Similarly, optical power combiners are essential for signal aggregation, upstream transmission, and balanced network design. In this article, we propose the design of two power splitters—3 dB and 6 dB Y-shaped configurations—that also function as power combiners using two-dimensional photonic crystal waveguides. The performance of these devices has been analyzed using the finite difference time domain (FDTD) algorithm, and their operational parameters have been optimized through the K-means clustering and Particle Swarm Optimization algorithms. As a result of this optimization, the devices achieve precise 3 dB and 6 dB power splitting across all output ports with an efficiency of 99 %. Their fast response time (0.4 and 0.5 picoseconds for 3 dB and 6 dB respectively), high power delivery efficiency, precise power splitting/combining capabilities, and Machine Learning (ML) – driven optimization make these splitters/combiners highly suitable for advanced fiber optic networks.

## 1. Introduction

Over the past decade, the field of communication has seen significant advancements, particularly in faster data transfer, reduced propagation loss, enhanced bandwidth, and improved signal-to-noise ratios. These improvements are largely attributed to the introduction of fiber optic networks. Optical fiber communication systems have surpassed microwave communication systems due to their intrinsic advantages, such as ultra-high bandwidth, low electromagnetic interference, minimal propagation loss, low cost per channel, and high transmission security. However, one major challenge remains: signal processing terminals, which require the conversion between optical and electronic signals, as they rely on electronic components. To address this bottleneck, researchers have been developing all-optical signal processing devices for photonic integrated circuits (PICs) (Yablonovitch, 1987). Various optical technologies, such as semiconductor optical amplifiers (SOA) (Runser et al., 2001), self-phase modulation (Tomlinson et al., 1984), cross-phase modulation (Olsson et al., 2000), Raman scattering (Sen and Das, 2013), self-collimation (Noori et al., 2017), plasmonics (Das and Mondal, 2024), and photonic crystals (PhC) (Parandin et al., 2021), have been explored to design these devices. Among these, photonic crystals are particularly promising due to their ability to control light propagation through a unique phenomenon known as the photonic band gap, which defines the transmission and reflectance characteristics of the crystal (Joannopoulos et al., 2008). In recent decades, significant research has focused on the development of photonic crystal-based devices such as optical routers (Thirumaran et al., 2021), demultiplexers (Mondal et al., 2019; Tekeste and Yarrison-Rice, 2006), decoders (Mondal et al., 2019; Serajmohammadi et al., 2015), power splitters/combiners (Ahmed et al., 2013), couplers (Dutta et al., 2016), logic gates (Farmani et al., 2019; Karami et al., 2024; Parandin et al., 2024; Karami et al., 2025; Fu et al., 2013; Tang et al., 2014), optical adder (Xavier et al., 2013; Karami et al., 2025; Jiang et al., 2015) and drop filters (Prakash et al., 2018). Among these, optical power splitters/combiners are essential components in advanced fiber optic networks. These devices play a crucial role in optical signal processing by dividing a single

* Corresponding author.
*E-mail addresses:* kalyanghosh042@gmail.com (K.K. Ghosh), mandal.haraprasad@gmail.com, mondal.haraprasad@dibru.ac.in (H. Mondal), das.himanshu69@gmail.com (H.R. Das), m.soroosh@scu.ac.ir (M. Soroosh), sudipta2020@dibru.ac.in (S. Majumder), bhargab@dibru.ac.in (B. Saikia).

https://doi.org/10.1016/j.rio.2025.100858
Received 30 December 2024; Received in revised form 27 April 2025; Accepted 7 June 2025
Available online 9 June 2025

optical signal across multiple waveguides or combining multiple signals into one waveguide. Optical power splitters, in particular, expand network capacity by distributing signals in both balanced and unbalanced ways according to network requirements. Conversely, optical power combiners merge signals from various network paths into a single backbone waveguide, facilitating long-distance communication and reducing overall network costs (Keiser, 2021; Agrawal, 2010; Ramaswami et al., 2009).

Due to the critical role of optical power splitters/combiners in optical networks, significant research efforts have been directed towards their design, resulting in numerous publications over the past few decades. For instance, Sohrabi et al. (2014) have reported a 1 × 3 power splitter based on a two-dimensional rods-in-air photonic crystal (PC) structure, utilizing two ring resonators. In their design, the inner rods of the ring resonators were assigned a refractive index of 1.009, with an operating wavelength of 1876 nm, which falls outside standard optical communication wavelengths. At this wavelength, the device achieves only 75 % power transfer at the output ports, with each output receiving merely 25 % of the input power. Similarly, Mohammadi and Mansouri-Birjandi (2015) have proposed a 1 × 5 optical power splitter using PC structures, based on the principle of directional coupling. The radii and refractive indices of the coupling rods have been set at 120 nm, 83 nm, and 2.5, 2 respectively. However, their results indicated unequal power distribution among the output ports, and the use of three different refractive indices within a single PC structure proved challenging. Mesri and Alipour-Banaei (2017) have designed a 1 × 4 power splitter employing directional coupling, achieving moderate efficiency with 88 % power transfer (22 % per output). Saral et al. (Betsy Saral et al., 2016) have reported 1 × 2 and 2 × 4 splitters using a square lattice configuration of 2D-PC structures with simple Y-shaped waveguides. However, these designs were hampered by inefficient performance at standard communication wavelengths and unequal power distribution at the outputs. Azar et al. (2018) have developed a 1 × 4 power splitter by optimizing the radii of six corner rods via a successive approximation method, achieving 99 % power transmission at the output ports. Meanwhile, Arunkumar et al. (2019) have presented 1 × 4 and 1 × 6 power splitters using 2D-PC rods in air structures, with operating wavelengths ranging from 1440 nm to 1505 nm. However, these devices were unsuitable for wavelength division multiplexed (WDM) networks centered around the 1550 nm communication wavelength. Rafiee et al. (2018) have introduced a 1 × 3 power splitter combining plasmonic effects with PC-based waveguides, embedding aluminum, silver, and copper rods near the output ports. Although effective at 1100 nm, 1209 nm, 1215 nm, and 1600 nm, the design was incompatible with the 1550 nm optical communication wavelength. Finally, Danaie et al. (2017) and Jindal and Kaur (2021) each have reported 1:2 power splitters based on holes-in-slab PC structures. While Danaie's design transmitted 90 % of input power, Poonam's device is designed for the near-infrared range and was not optimized for optical networks operating at the 1550 nm center wavelength.

The reports mentioned above have significantly advanced the design of optical power splitters and combiners; however, there remains considerable potential for further optimization, improved efficiency, and size reduction. In pursuit of these objectives, 1:2 (3 dB) and 1:4 (6 dB) power splitters with Y-shaped configurations and negligible design complexity have been designed using a two-dimensional rods-in-air photonic crystal structure. To enhance efficiency, certain parameters within the waveguides were optimized using machine learning algorithms, and the devices' performance was evaluated. Additionally, the same structures have been repurposed as power combiners (2:1 and 4:1) by reversing the input and output ports. Following the introduction, in section 2, the numerical design and theory behind the PhC based devices are discussed. The architectural design of the proposed devices and their energy band diagrams are presented in the next section. Section four provides an analysis of the performance and results, including a discussion on various loss measurement techniques. The three-dimensional design and analysis have been presented in section five. Furthermore, the optimization of device performance using machine learning algorithms is elaborated in the next section. Finally, the conclusions of this work are summarized in the last section.

## 2. Numerical design and theory

Due to ease of manufacture, 2D PhCs are seen to be the most promising platform for building optical devices. A few key optical characteristics make up PhCs, which have a wide range of practical uses. Primarily, PhC structures are polarization dependent. Second, PBG—a gap between the continuums of states—is present in PhC structures. In PhC, transmittance happens for frequencies other than the band gap, while band gap frequencies are reflected from the crystal. Third, polarization and material characteristics affect a PhC's bandgap position and width. Lastly, by simply defecting, changing, or adjusting the PhC crystal lattice, more modes can be produced inside the PhC's band.

Calculating the propagation of light waves in PhC structure and analyzing the full photonic band gap in a periodic dielectric medium can be done by solving a master equation (Joannopoulos et al., 2008) that is derived from Maxwell's equations. The following derivation of the master equation uses the same equations, symbolic notations, and conventions that were reproduced from (Joannopoulos et al., 2008; Jamois et al., 2003; Sukhoivanov and Guryev, 2009; Sakoda, 2005). The dielectric, isotropic, and linear media Maxwell's equations are expressed as follows:

$$\nabla \bullet \mathrm{D}(\mathrm{r},\mathrm{t}) = 0 \tag{1}$$

$$\nabla \bullet \mathrm{B}(\mathrm{r},\mathrm{t}) = 0 \tag{2}$$

$$\nabla \times \mathrm{E}(\mathrm{r},\mathrm{t}) = -\frac{\partial \mathrm{B}(\mathrm{r},\mathrm{t})}{\partial \mathrm{t}} \tag{3}$$

$$\nabla \times \mathrm{H}(\mathrm{r},\mathrm{t}) = \frac{\partial \mathrm{D}(\mathrm{r},\mathrm{t})}{\partial \mathrm{t}} \tag{4}$$

where the vectors for the electric field, magnetic field, electric displacement, and magnetic flux density are denoted by E(r,t), H(r,t), D (r,t), and B(r,t), respectively. Additionally, the electric field and current density (J) can be connected as –

$$\mathrm{J} = \sigma \mathrm{E}. \tag{5}$$

For non-magnetic materials, the permeability (μ) is equivalent to the free-space permeability ($\mu_0$), and the relationship between B(r,t) and H (r,t) is expressed as –

$$\mathrm{B}(\mathrm{r},\mathrm{t}) = \mu_0 \mathrm{H}(\mathrm{r},\mathrm{t}). \tag{6}$$

Additionally, permittivity (ε(r)) determines the relationship between D (r,t) and E(r,t), and for an isotropic, spatially periodic material, this relationship is –

$$\mathrm{D}(\mathrm{r},\mathrm{t}) = \varepsilon_0 \varepsilon(\mathrm{r}) \mathrm{E}(\mathrm{r},\mathrm{t}) \tag{7}$$

where the free-space permittivity is denoted by $\varepsilon_0$. Currently, by replacing Eqs. (3) and (4) with Eqs. (6) and (7), we obtain –

$$\nabla \times \mathrm{E}(\mathrm{r},\mathrm{t}) = -\mu_0 \frac{\partial \mathrm{H}(\mathrm{r},\mathrm{t})}{\partial \mathrm{t}}, \tag{8}$$

$$\nabla \times \mathrm{H}(\mathrm{r},\mathrm{t}) = \varepsilon_0 \varepsilon(\mathrm{r}) \frac{\partial \mathrm{E}(\mathrm{r},\mathrm{t})}{\partial \mathrm{t}}. \tag{9}$$

Now, Eqs. (8) and (9) are coupled equations and Eqs. (8) and (9) can be rewritten as –

$$\frac{1}{\varepsilon(\mathrm{r})} \nabla \times \{\nabla \times \mathrm{E}(\mathrm{r},\mathrm{t})\} = -\frac{1}{\mathrm{c}^2} \frac{\partial^2 \mathrm{E}(\mathrm{r},\mathrm{t})}{\partial \mathrm{t}^2}, \tag{10}$$

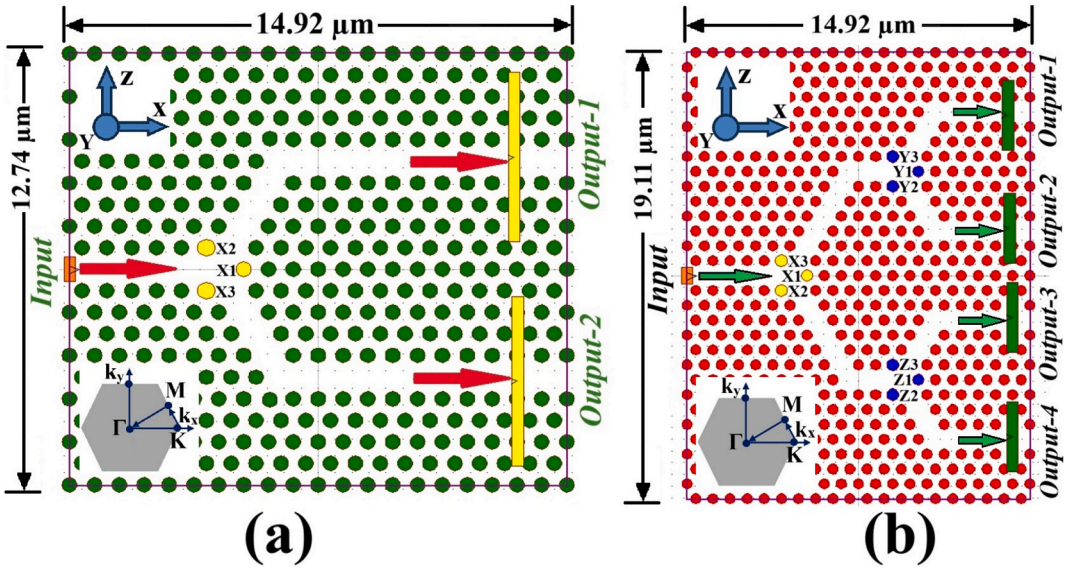


**Fig. 1.** Schematic diagram of (a) 1: 2 optical power splitter "and" (b) 1:4 optical power splitter.

$$\nabla \times \left\{ \frac{1}{\varepsilon(r)} \nabla \times H(r,t) \right\} = -\frac{1}{c^2} \frac{\partial^2 H(r,t)}{\partial t^2}, \tag{11}$$

Where, $c = \frac{1}{\sqrt{\mu_0 \varepsilon_0}}$ free space velocity of light wave. In time-harmonic forms, the electric and magnetic fields can be expressed as –

$$E(r,t) = E(r)e^{-i\omega t}, \tag{12}$$

$$H(r,t) = H(r)e^{-i\omega t}, \tag{13}$$

where angular frequency is denoted by ω. The following equations are produced by substituting Eqs. (12) and (13) into Eqs. (10) and (11). We call these the master equations.

$$\frac{1}{\varepsilon(r)} \nabla \times \{ \nabla \times E(r) \} = \frac{\omega^2}{c^2} E(r), \tag{14}$$

$$\nabla \times \left\{ \frac{1}{\varepsilon(r)} \nabla \times H(r) \right\} = \frac{\omega^2}{c^2} H(r). \tag{15}$$

## 3. Architectural design of power splitters/combiners

In this section, the detailed architectural design and band structure of the PC material in defect mode and non-defect mode have been discussed. Initially, 21 × 21 and 21 × 31 arrays of silicon rods arranged in hexagonal lattice have been taken to design 1:2 and 1:4 optical power splitter/combiner respectively. However, the dimensions of the base sutuctures for the 1:2 and 1:4 power splitter/combiner have been measured as 190 µm2 and 288 µm2 respectively. For both the devices, the dielectric constant (ε), the radius of the rods, and the lattice constant ('a') of the PC platform have been chosen as 11.9, 220 nm, and 735 nm respectively. For designing a 1:2 power divider, one input waveguide and two output waveguides (altogether form a Y-shaped waveguide) have been created by removing rods in Γ-M direction as shown in Fig. 1a. To reduce the back reflection of the signal at the junction and to deliver the maximum power to the output port, the radii of three rods namely X1, X2, and X3, adjacent to the junction have been optimized as 200 nm, 254 nm, and 254 nm respectively. On the other hand, for designing 1:4 power splitters, three Y-junctions have been created (by removing rods in Γ-M direction) in a cascade manner as shown in Fig. 1b. The radii of all the rods adjacent to the junctions (X1, X2, X3 and Y1, Y2, Y3, and Z1, Z2, Z3) have been optimized to minimize the back

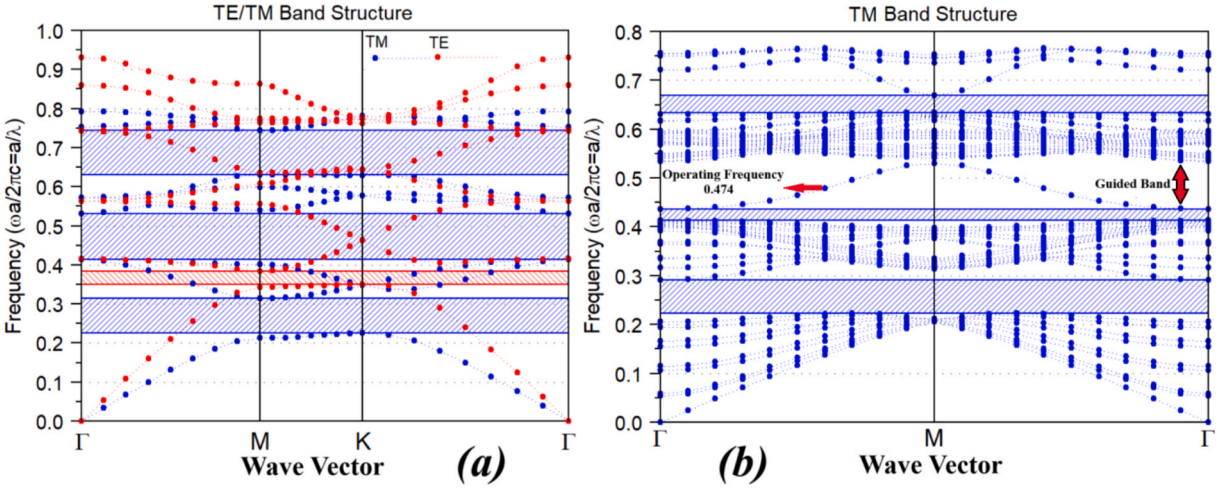


**Fig. 2.** (a) Complete photonic band structure of non-defect PhC "and" (b) Projected band diagram of defect PhC.

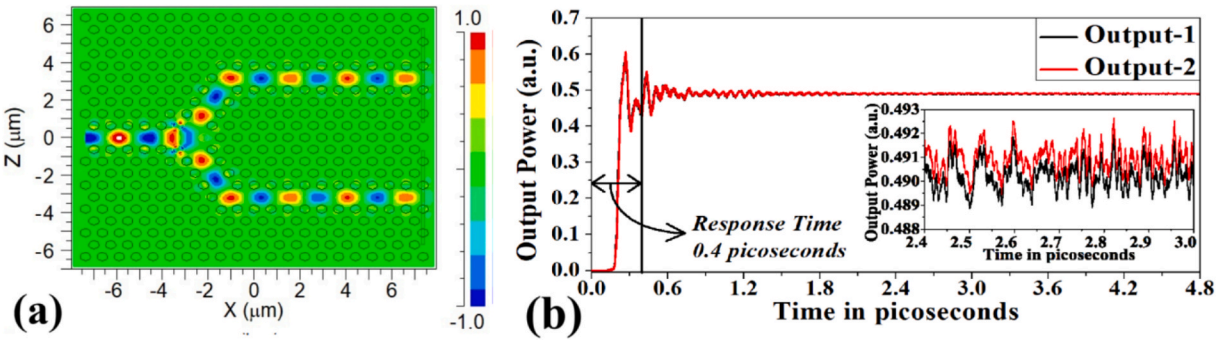


**Fig. 3.** (a) Electric field propagation profile "and" (b) Time evolving graph, of 1:2 power splitter.

reflection at the junctions and transfer maximum power to the output ports. The radius of 241 nm has been set for the rods, X1, Y1, and Z1, whereas the radius of 285 nm has been set for the rods, X2, X3, Y2, Y3, Z2, and Z3 respectively. Moreover, to make the proposed structures function as optical power combiners, the signals must be applied at the output ports and the combined signal can be obtained at the input port of the proposed structures.

Furthermore, the full photonic band gap (PBG) of the non-defect PC structure for both transverse electric (TE) and transverse magnetic (TM) modes has been computed using the plane wave expansion (PWE) method (Prather et al., 2009), as shown in Fig. 2a where three complete PBG and one complete PBG have been found in TM and TE modes respectively. In TM mode the PBG is found in the normalized frequency (a/λ) range of 0.225 to 0.315 (wavelength range of 2333 nm to 3266 nm), 0.414 to 0.53 (wavelength range of 1386 nm to 1775 nm) and 0.63 to 0.745 (wavelength range of 986 nm to 1166 nm), whereas in TE mode a small PBG is obtained in normalized frequency (a/λ) between 0.35 and 0.385 (wavelength range of 1910 nm to 2100 nm). After obtaining the complete PBG it is realized that the center wavelength of standard optical communication, 1550 nm falls approximately in the center of the second band in TM mode which ranges between 1386 nm and 1770 nm. However, to control the flow of light and guide the propagation of optical waves, the waveguide is designed by eliminating a line of rods in the X-direction (Γ-M) of the PC structure. Additionally, to find the waveduide's frequency states the projected band diagram has been calculated by utilizing the PWE algorithm only in the Γ-M direction making the waveguide symmetry in the Y-direction as shown in Fig. 2b. However, the Fig. 2b it is observed that only the projected band is found in TM mode in the wavelength range of 1400 nm to 1670 nm, which proves that the waveguide, designed in PC structure is well suited to guide and propagate optical waves within it.

## 4. Result discussion and performance analysis

The finite difference time domain (FDTD) algorithm (Johnson and Joannopoulos, 2001) has been utilized to get the results and to measure the various performance matrices of the proposed devices. This section also depicts the comparative analysis with the existing literature based on the design and performance aspects. However, the Perfectly Matched Layers (PML) absorbing border condition has been used in order to precisely calculate the signal power distribution. To assess the performance and functionality of the suggested power splitters, a Gaussian optical monochromatic source generating continuous wave (CW) of TM polarization at a wavelength of 1550 nm (with a fixed power level of 1 $\mu W/\mu m^2$) is applied at the input port. Moreover, few critical parameters like the radius of the rods, lattice constant (pitch), refrective index of the material (based on which FDTD simulation algorithm performs) have been chosen as 220 nm, 735 nm and 0.45 respectively. A line monitor placed at the output port is used to measure the optical intensity at the outputs. The wavelength of the signal determines how tiny the spatial grid needs to be in order to guarantee a thorough simulation. The electric field propagation profiles and time-evolving graphs, obtained from the FDTD method have been shown in Fig. 3 and Fig. 4 for 1:2 and 1:4 power splitters respectively. From Fig. 3b, it is proved that the proposed 1:2 power splitter can split the input optical signal power with an equal proportion of 0.492 of input power at both the output ports. Therefore, with a simple structure (only altering the radii of three rods X1, X2, and X3) the transmission efficiency is obtained as 99 %. The electric field propagation profile of the 1 × 2 power splitter has been recalculated by applying FDTD algorithm where grid size is reduced by half. Initially, the parameters like time step, grid spacing, have been taken as 0.072 fs, Dx = 10 nm Dz = 10 nm respectively which have changed to 0.036 fs, Dx = 5 nm Dz = 5 nm. It is observed from simulation that, both the output deliver 0.47 of input power, which establish the output power efficiency of 94 %. Therefore, the convergence error percentage can be calculated as 5 %.

Moreover, by using the FDTD algorithm the performance of the structure, (shown in Fig. 1a as an optical power combiner) has been examined. For this case, the power monitor is placed near to input port, and two optical power sources with continuous waves (Gaussian

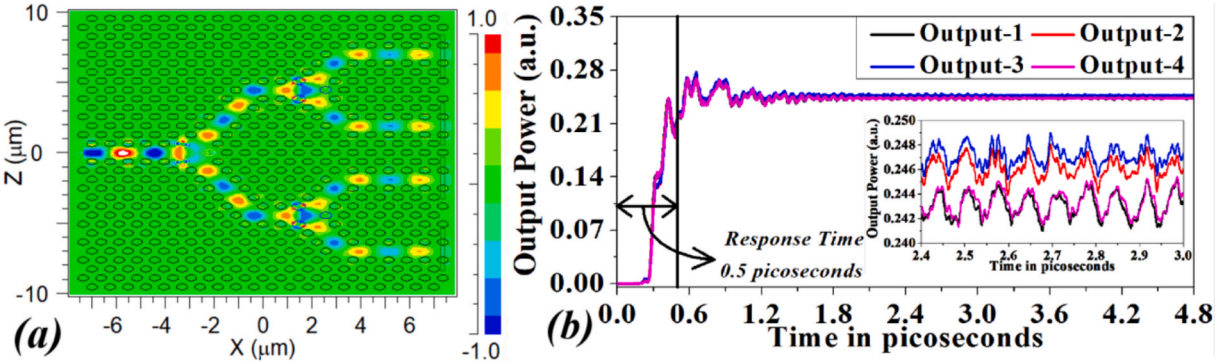


**Fig. 4.** (a) Electric field propagation profile "and" (b) Time evolving graph, of 1:4 power splitter.

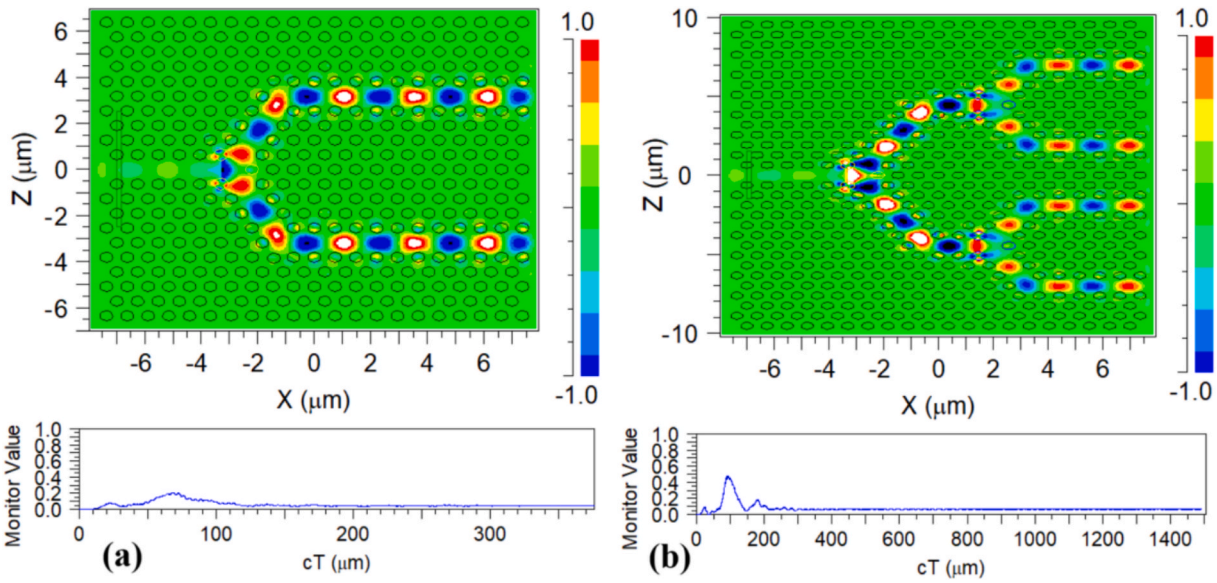


**Fig. 5.** Return loss profile of (a) 1:2 power splitter "and" (b) 1:4 power splitter.

Shaped) having a power level of 1 μW/μm$^2$ have been applied at both the output ports. As a result, 99 % optical power (1.98 μW/μm$^2$) is coupled at the junction and reaches the input port.

Additionally, from the time-evolving graph, depicted in Fig. 4b, it is evident that the proposed 1:4 power splitter is capable of dividing the optical signal power applied at the input port with equal proportion to all the output ports. Moreover, the optical power level at the output ports has been measured as 0.245 μW/μm$^2$, which establishes the transmission efficiency of 98 %. Moreover, a 1:4 power splitter has also been examined as a power combiner by applying an optical source at the output ports and an optical power monitor at the input port. From this analysis it is observed that a total of 98 % optical power (3.93 μW/μm$^2$)) is combined and reaches the input port.

However, in this section, a few performance matrices of power splitters have also been discussed. One of the most important metrics for evaluating the functionality of optical devices is return loss (RL). The return loss, which is expressed in dB, is calculated by dividing the light applied into the device by the light reflected back toward the source. Return loss can be stated mathematically as:

$$RL = 10Log_{10}\frac{P_{input}}{P_{return}} \tag{16}$$

where $P_{return}$ indicates the power of the signal reflected back at the input port, and $P_{input}$ indicates the signal power delivered at the input port. For the best device performance, a large return loss is preferred since it denotes increased efficiency and reduced signal reflection (Anagha and Jeyachitra, 2022). Both of the suggested devices' return losses have been calculated. To calculate the return loss for both 1:2 and 1:4 power splitters, the optical sources are placed five periods inside the input waveguide for both devices and the optical power monitors are placed just at the starting of the input ports. The reflected power (Preturn) for both devices has been measured as 0.002 × Pinput and 0.004 × Pinput for 1:2 and 1:4 power splitters, respectively (as shown in Fig. 5). To calculate the return loss for 1:2 power splitter, the Pinput = 1 and Preturn = 0.002 have been considered and substituted in the Eq. (16):

$$RL = 10Log_{10}\frac{1}{0.002} = 10Log_{10}(500) = 26.9897\,dB$$

Moreover, to calculate the return loss for a 1:4 power splitter, the Pinput = 1 and Preturn = 0.004 have been measured and substituted in the Eq. (16):

$$RL = 10Log_{10}\frac{1}{0.004} = 10Log_{10}(250) = 23.9794\,dB$$

Therefore, using Equation (16), the return losses for 1:2 and 1:4 power splitters have been found to be approximately 27 dB and 24 dB, respectively. Moreover, in photonic crystal waveguides (PCWs), back reflection can impair signal integrity, lower transmission efficiency, and perhaps interfere with normal laser operation at the source. Back reflection in PCWs can be reduced by using a few efficient strategies. First and foremost, impedance matching and reflection reduction can be aided by the application of thin-film coatings at the waveguide interface with a precisely selected refractive index. Second, undesired reflections can be absorbed by integrating materials with regulated optical loss at the edges or by employing absorptive boundary layers. Additionally,

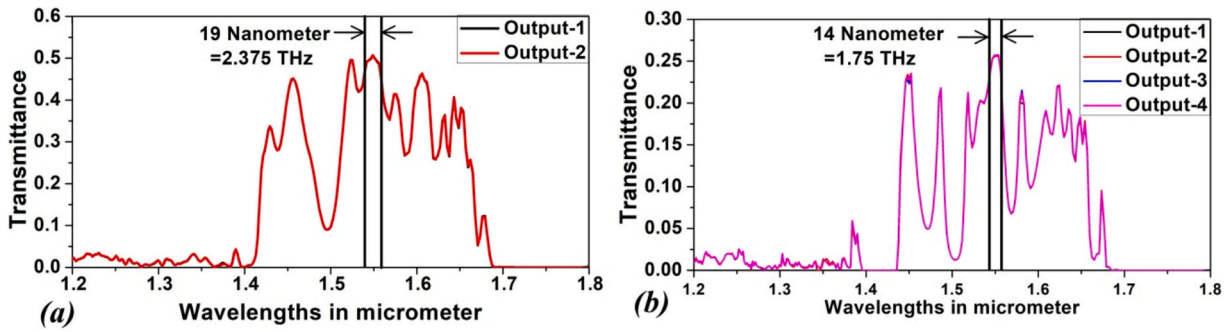


**Fig. 6.** Transmittance of proposed (a) 1x2 power splitter, "and" (b) 1x4 power splitter.

**Table 1**
Comparative analysis with published power splitters.

| Ref. | Structure Used | Operating Principle | Footprint ($\mu m^2$) | Resonance wavelength (nm) | Output Power Efficiency (%) |
|---|---|---|---|---|---|
| (Sohrabi et al., 2014) | Rods-in-air | Micro ring resonator and linear optics. (1 × 3) | 204 | 1876 | 60 |
| (Mohammadi and Mansouri-Birjandi, 2015) | Rods-in-air | Directional coupling and multimode interference in linear optics. (1 × 5) | 2500 | – | – |
| (Mesri and Alipour-Banaei, 2017) | Rods-in-air | Directional coupling in linear optics. (1 × 4) | 160 | 1550 | 95 |
| (Betsy Saral et al., 2016) | Rods-in-air | Heterostructure based design in linear optics. (1 × 2 and 1 × 4) | 100 (1 × 2)<br>224 (1 × 4) | 1455 (1 × 2)<br>1436 (1 × 4) | 100 (1 × 2)<br>70 (1 × 4) |
| (Azar et al., 2018) | Rods-in-air | T-junction with defect in the corners and in linear optics. (2-inputs) | 130 (1 × 2)<br>130 (1 × 4) | 1550 | 99.6 (1 × 2)<br>99 (1 × 4) |
| (Arunkumar et al., 2019) | Rods-in-air | Heterostructure based design in linear optics. (1 × 2, 1 × 3, 1 × 4 and 1 × 5) | 130 (1 × 2 and 1 × 3)<br>275 (1 × 4)<br>357 (1 × 6) | 1520 (1 × 2)<br>1475 (1 × 3)<br>1460 (1 × 4)<br>1495 (1 × 6) | 100 (1 × 2)<br>90 (1 × 3)<br>97 (1 × 4)<br>95 (1 × 6) |
| (Rafiee et al., 2018) | Rods-in-air | Multimode interference in plasmoni & PhC based mixed structure. (1 × 3) | – | 1100<br>1209<br>12151600 | – |
| (Danaie et al., 2017) | Rods-in-air andHoles-in-slab | Micro-cavity in linear optics. (1 × 2 T-shapped and 1 × 2 Y-shapped) | 50 (T-shapped)<br>33 (Y-shapped) | 1550 | 98 (T-shapped)<br>90 (Y-shapped) |
| (Jindal and Kaur, 2021) | Holes-in-slab | Micro-cavity in linear optics (1 × 2) | 100 | 1430 | 97 |
| **This work** | Rods-in-air | Simple Y-jounction in linear optics and optimization using ML algorithm. (1 × 2 and 1 × 4) | 190 (1 × 2)<br>288 (1 × 4) | 1550 | 99 (1 × 2)<br>99 (1 × 4) |

chirping—a steady change in the photonic crystal lattice's periodicity—can lessen abrupt changes that result in reflection and aid in impedance matching. Lastly, scattering is reduced by adjusting the photonic crystal structure's defect size and form and using gently curved bends rather than abrupt corners can assist in minimizing back reflection and mode mismatch.

Another vital metrice to measure the performance of an optical device is response time. It is defined as the transmission time of a wave to reach the output port of the device from its initial value to 90 % of the steady state of its final value. Response time is the sum of transition time and SteadyState time. Transition time is the time for a wave to reach from the input of a device to just at the output whereas steady state time is the time for a signal to reach 90 % of its steady state value. From the time-evolving graphs, depicted in Fig. 3b and 4b, the response times of 1:2 and 1:4 power splitters/combiners have been calculated as 0.4 and 0.5 picoseconds.

When assessing the performance of any all-optical device, transmittance is an essential characteristic. The transmittance for both devices has been examined in our study, taking into account all of the output ports. By measuring the optical signal power at the output port for various input wavelengths, transmittance may be determined. The transmittance for a 1 × 2 power divider with an input signal wavelength ranging from 1200 to 1800 nm is shown in Fig. 6a. The wavelength at which the highest transmittance is observed is 1550 nm. The transmittance for a 1 × 4 power divider is similarly shown in Fig. 6b, where the input signal wavelength ranges from 1200 to 1800 nm. The wavelength at which the highest transmittance is observed is 1550 nm. Furthermore, the 1 × 2 power divider exhibits nearly maximum output power within the wavelength range of 1540 to 1559 nm, implying a bandwidth of roughly 2.375 THz. Comparably, the 1 × 4 power divider exhibits nearly maximum output power within the wavelength range of 1543 to 1557 nm, implying a bandwidth of roughly 1.75 THz. Thus, for 1 × 2 and 1 × 4 power dividers, the resonance wavelength range derived from Fig. 6 is 1540 nm to 1559 nm and 1543 nm to 1557 nm, respectively. These transmittance properties guarantee that the suggested power dividers can operate effectively over the whole C-band, which is utilized in telecommunications systems.

Furthermore, as indicated in Table 1, a thorough examination has been carried out by consulting the text of available literature. Table 1 shows that, with the exception of Jindal and Kaur (2021), practically all of the published works (Keiser, 2021; Agrawal, 2010; Ramaswami et al., 2009; Sohrabi et al., 2014; Mohammadi and Mansouri-Birjandi, 2015; Mesri and Alipour-Banaei, 2017; Betsy Saral et al., 2016; Azar et al., 2018) make use of rods-in-air structures. The devices described in (Sohrabi et al., 2014; Mohammadi and Mansouri-Birjandi, 2015; Mesri and Alipour-Banaei, 2017; Danaie et al., 2017; Jindal and Kaur, 2021) have a long response time because they primarily rely on the concepts of directional couplers and micro ring resonators. Moreover, from Table 1, it has been observed that, the devices reported in (Sohrabi et al., 2014; Betsy Saral et al., 2016; Arunkumar et al., 2019; Rafiee et al., 2018; Jindal and Kaur, 2021) are unable to operate in standard optical communication wavelength, which indicate that these devices are not suitable as signal processing devices of WDM/DWDM (Wavelength Division Multiplexed/ Densed Wavelength Division Multiplexed) system. However, our suggested devices' operating wavelengths are in good alignment with the wavelength of conventional optical communication. Furthermore, these designs are rather straightforward and operate as power splitters with 99 % output power efficiency.

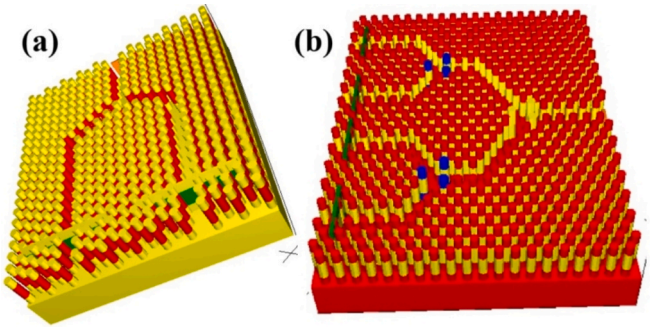


**Fig. 7.** Three-dimensional representation of (a) 1 to 2 power divider, "and" (b) 1 to 4 power divider.

## 5. Three-dimensional analysis

To realize the practicality of any real device should have a finite height. In this section, the three-dimensional design and performance of the proposed power splitters have been discussed. As these devices are made in the PhC structure of rods in air, for mechanical support of all the silicon rods a slab of silica (SiO2) having a height of 1 μm has been taken. The total height of the devices is chosen as 2 μm where the supporting slab/ base slab is 1 μm and the rod's height is 1 μm. The height of the 1-

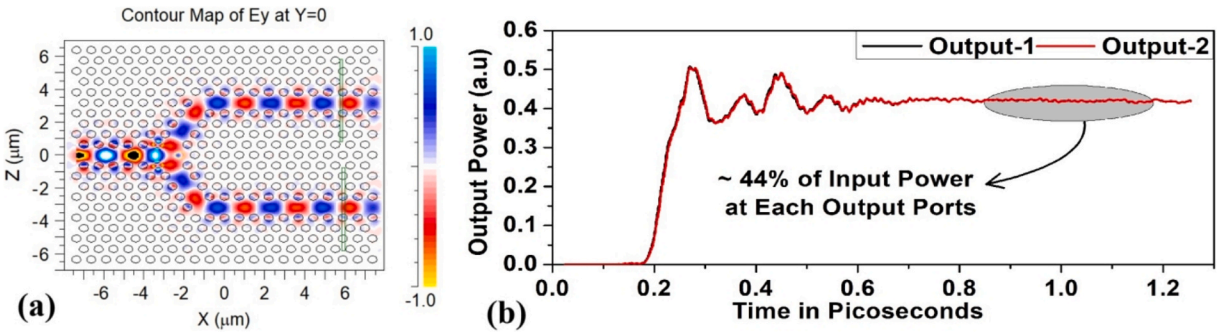


**Fig. 8.** (a) 3D-FDTD electrical field propagation profile "and" (b) Time evolving graph of 3D-FDTD simulation, of 1 to 2 line power divider.

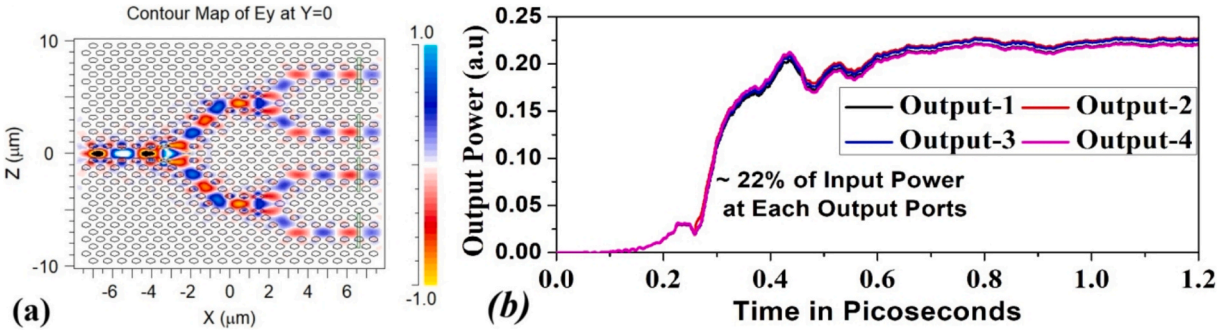


**Fig. 9.** (a) 3D-FDTD electrical field propagation profile "and" (b) Time evolving graph of 3D-FDTD simulation, of 1 to 4 line power divider.

μm rod is further divided into three layers, they are considered as a top layer, a bottom layer, and a middle/propagation layer as shown in Fig. 7. To make the vertical symmetry (Y-direction) top and bottom layer is made with silica (SiO2) as the bottom layer is fixed to the supporting layer which is made with silica. The height of top and bottom layers is set as 0.2 μm each and the height of the propagation layer is considered

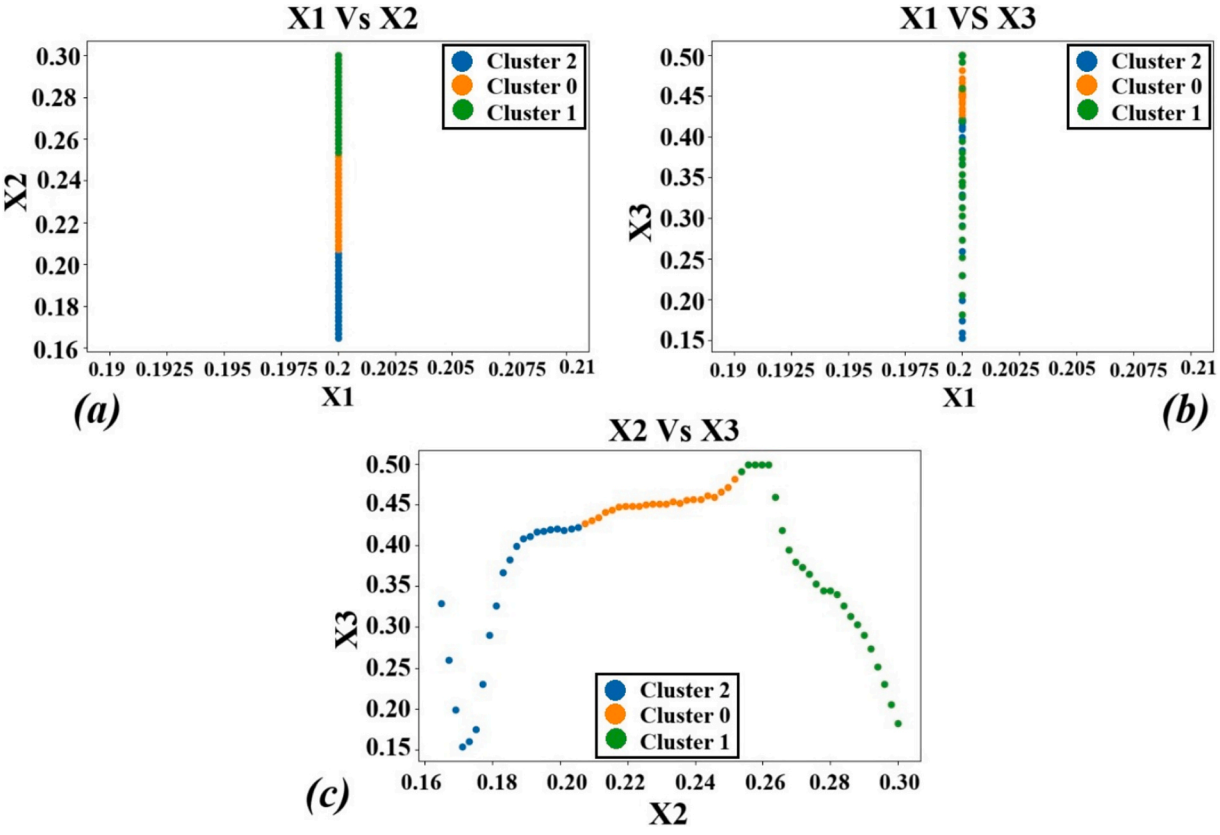


**Fig. 10.** (a) Plot of x2 with respect to x1 "and" (b) Plot of x3 with respect to x1 "and" (c) Plot of x3 with respect to x2.

**Table 2**
Proposed K-Means and PSO-Based Optimization Algorithm.

**Input:** A data set D which has three columns namely $x_1, x_2, x_3$ where $x_1$ and $x_2$ are features namely center rod radius and adjacent rod radius respectively, and $x_3$ is the output power to be maximized. Parameters used:
- K is the numbers of clusters for clustering.
- lb (lower bounds for $x_1, x_2$) and ub (upper bound for $x_1, x_2$) are the bounds used for optimization.

**Output:**
- $-x_3^{\max}$ presents the maximum value of output power ($x_3$).
- $-x_1, x_2$ are the corresponding value of center and adjacent rod radius respectively which produces $x_3^{\max}$.

**Algorithm:**
**Stage 1:**
Objective: To select clusters' number K by minimizing the width in the cluster sum of squares (WCSS)
a. For each K
Compute WCSS: $WCSS(K) = \sum_{i=1}^{k} \sum_{d_j \in c_i} \|d_j - c_i\|_2^2$ Eq. A
b. Plot WCSS (K) vs K
c. Identify the "elbow point" where WCSS decreases rapidly and then stabilizes.
**Stage 2:**
Objective: To partition D into K clusters.
a. Select K initial centroid randomly, C={ $c_1, c_2, \ldots\ldots, c_k,$ } where $c_i=(x_{1i}, x_{2i})$
b. For each $d_j = (x_{1i}, x_{2i}) \in$ D:
- Assign $d_j =$ to the cluster $i$ with the centroid

Cluster $(d_j) = \arg\min ||d_j - c_i||_2$ Eq. BWhere $||d_j - c_i||_2 = \sqrt{(x_{1j} - x_{1i})^2 + (x_{2j} - x_{2i})^2}$ Eq. C
c. For each cluster i, read compute the centroid.
$c_i = \frac{1}{|c_i|} \sum_{d_j \in c_i} d_j$ Eq. DWhere $|c_i|$ is the number of points in cluster i.
d. Continue step B and C until the centroids do not change significantly.
$\Delta C = max_i \left\| c_i^{(t)} - c_i^{(t-1)} | \right|_2 <\in$ Eq. EWhere $\in$ is a small threshold
e. The final cluster and centroid C= {$c_1, c_2, \ldots\ldots, c_k,$}
**Stage 3:**
Objective: To maximize $x_3$ by optimizing $x_1 and x_2$
a. Define bonds such that
lb = (min($x_1$), min($x_2$))ub = (max($x_1$), max($x_2$))Initialize n particles randomly within bonds$P_i$ ($x_{1i}, x_{2i}$), v ($v_{1i}, v_{2i}$)Where $P_i$ is the position, $V_i$ is the velocity of the $i^{th}$ particle
b. For a particle position P = $(x_1, x_2)$
Find f (p) = $-x_3(P)$Where -$x_3(P)$ is the $x_3$ for the closest data point.Closest point (P) = $\arg min_j \|P\text{-}(x_{1j}, x_{2i})\|_2$ Eq. F
c. For each particle i:
$V_i = \omega V_i + C_1\gamma_1\left(P_i^{best} - P_j\right) + C_2\gamma_2\left(G^{best} - P_i\right)$ Eq. G$P_i = P_i + V_i$ Eq. HWhere
- ω: inertia weight
- $C_1$, $C_2$: acceleration coefficients
- $\gamma_1, \gamma_2$ : random values in [0,1]
- $P_i^{best}$: particles best known position
- $G^{best}$: global best position

d. Track the global best fitness $G^{best}$ over iteration
e. Optimize output $P^{best} = (x_1^{best}, x_2^{best})$ and its corresponding maximum $x_3^{best} = -f(P^{best})$
**Stage 4:**
Objective: To check if $P^{best}$ exists in the data set.
a. Compute the closest point to $P^{best}$.
Closest point $(P^{best}) = \arg min_j \|P^{best} - (x_{1i} - x_{2i})\|_2$
b. If the closest point matches $P^{best}$ within tolerance, confirm the match.

as 0.6 μm. Due to the advancement of semiconductor fab labs, the fabrication of these proposed structures is now possible. While various methods are available for the fabrication of complex photonic crystal (PC) structures. It is possible to execute the suggested layered 2D PC rods-in-air design utilizing techniques similar to the techniques reported in the articles (Bienstman et al., 2003; Assefa et al., 2004; Shih et al., 2008; Kok et al., 2006). Fabrication of the proposed device can be done by the following process flow. PECVD can be used to deposit a 200 nm SiO2, a 600 nm Si, and a 200 nm SiO2, chronologically, on a silicon substrate. Thereafter, a highly etch-resistant e-beam photoresist (eg, SML 300 by EMresist) may be used to define the mask through e-beam lithography. In this context, it would be worth mentioning that sub-50 nm patterns have been easily obtained through e-beam lithography in different laboratories (one can refer to the datasheet of SML 300). Thereafter, the masked wafer may be placed in a DRIE chamber for pattern transfer. A 20 W RF plasma on a successive 50 sccm gas flow of CF4, SF6, and CF4 under a 0.5 mTor chamber pressure is expected to be sufficient to transfer the desired pattern on the wafer. Although the aspect ratio of the device is large, the surface wall passivation in DRIE can successfully transfer the desired pattern. In light of the above, we believe that the fabrication of the proposed device is quite feasible in a standard CMOS fabrication laboratory.

Moreover, by applying the 3D-FDTD algorithm, the electric field propagation profiles with finite height structures have been observed (as shown in Figs. 8a and 9a). Further to measure the output powers of the proposed power dividers the time response graphs have been obtained. From time-evolving graphs, it has been observed that for a 1-to-2-line power divider, ~44 % of input power reaches both the output ports whereas for a 1-to-4-line power divider ~22 % of input power reaches all the output ports (shown in Fig. 8b and 9b respectively). According to the 3D-FDTD results, the suggested devices produce 3D structure (with finite height) results that are nearly identical to their 2D equivalent.

## 6. Output power optimization using ML algorithm

In this section, the detailed analysis of output power optimization of a 3 dB power divider using an ML algorithm has been presented. Initially, the radius of the rods (including x1, x2, and x3 as shown in Fig. 1a) is chosen as 220 nm. For output power optimization, the three center rods are clustered into two groups (x1 and x2, x3). Initially, the x1 rod's radius has been chosen as 200 nm and it has been varied up to 250 nm with the interval of 1 nm. Similarly, radii of x2 and x3 rods are simultaneously varied from 165 nm to 300 nm with an interval of 1 nm. In this work, the R-Soft CAD design tool has been used to design the device, and utilizing the Python program, multiple simulations of R-Soft CAD software have been performed keeping the certain values of radii of x1, x2, and x3. For example, keeping the value of x1 fixed at 200 nm, values of x2 and x3 have simultaneously varied from 165 nm to 300 nm

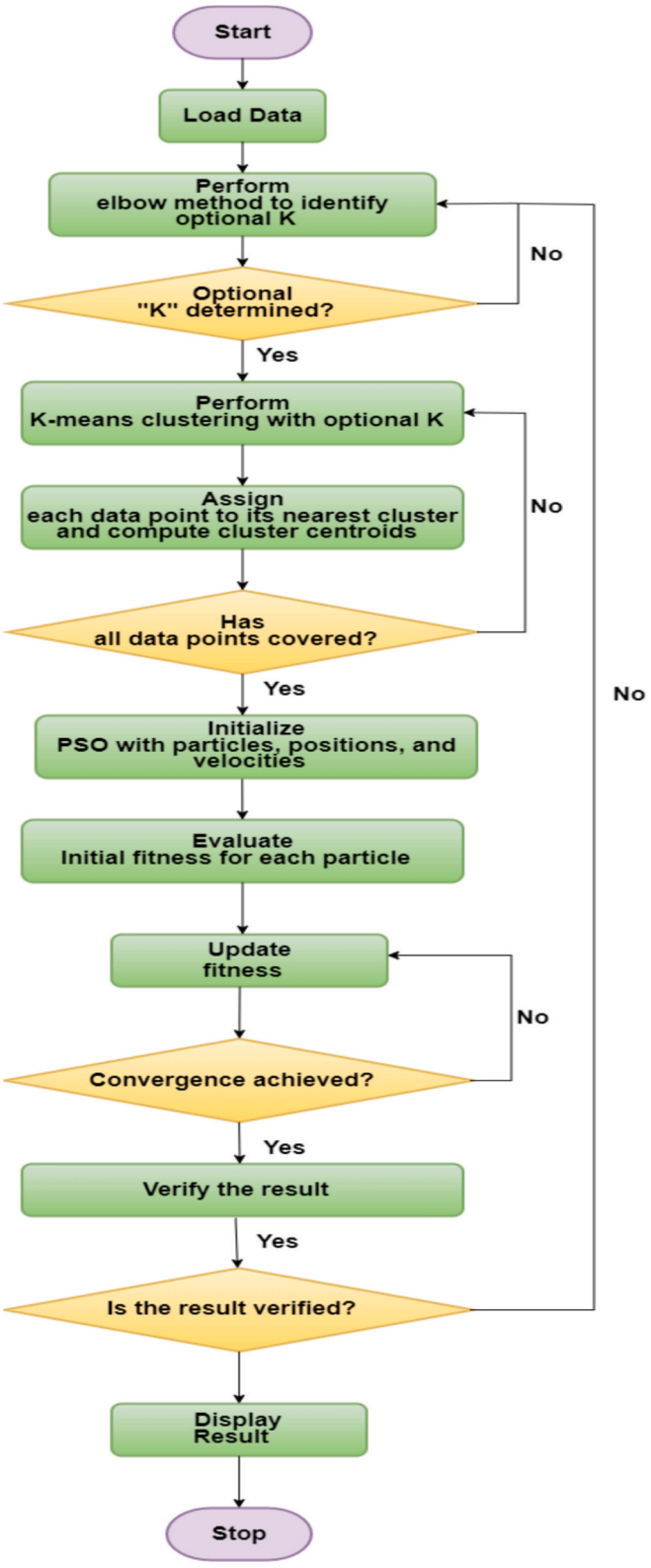


**Fig. 11.** Flow chart of proposed algorithm.

with an interval of 1 nm. This process has been continued for the value of x1 ranging from 200 nm to 250 nm with the interval of 1 nm and output power levels of the device for every value of x1 and x2, x3 have been recorded. In this process, the total dataset (D) has been generated. However, the values of X2 and X3 have been calculated with respect to various values of X1 as shown in Figs. 10a and 10b, respectively. The values of X3 have also been calculated with respect to various values of X2, which is shown in Fig. 10c.

The algorithm works on dataset D, which consists of three columns: two features $x_1$ (is known as x1 as per Fig. 1a) and $x_2$ (is known as x2, x3 as per Fig. 1a) a target variable $x_3$ (is considered as output power) whose maximum value needs to be chosen. The proposed algorithm, Table 2, works on the following stages:

**Stage 1:** The algorithm groups the data into K clusters. The elbow method is employed to find the optimal number of clusters (K). In this method, the Within-Cluster Sum of Squares (WCSS) is computed for each possible K, a measure of how compact the clusters are. A mathematical formula (Eq. A) is applied to calculate WCSS and the values are plotted against K. The optimal K is identified at the "elbow point" on the graph, where the WCSS curve drops and stabilizes. This ensures a good balance between simplicity and meaningful representation of the data.

**Stage 2:** Once the optimal K is determined, the dataset is divided into K clusters by using K-means clustering. The algorithm starts by randomly selecting K centroids from the dataset. After the step, each data point is assigned to the nearest centroid. This is determined using the Euclidean distance (Eq. B and Eq. C). After that, the centroids are recalculated as the mean of all points within the cluster (Eq. D). This process of reassigning points and recalculating centroids is repeated until the centroids' positions change by less than a defined threshold (∈), indicating convergence (Eq. E). At the end of this step, the algorithm produces the final clusters and their centroids.

**Stage 3:** After clustering, the algorithm focuses on optimizing the target variable by using a method called Particle Swarm Optimization (PSO). In this stage, the algorithm first establishes the bounds (lb and ub) for the search space based on the minimum and maximum values of $x_1$ and $x_2$ in the dataset. A group of "particles" is created, each with a random position and velocity within these bounds. The PSO process aims to maximize $x_3$, defined as a function f(P) at the position P of a particle. For each particle, $x_3$ is computed for the data point closest to P (Eq. F). The fitness of each particle, which corresponds to f(P) is then evaluated. The particles iteratively update their positions and velocities to improve their fitness. These updates depend on each particle's personal best position ($P_i^{best}$) and the global best position ($P_g^{best}$), guided by factors like inertia (ω\omega), acceleration coefficients ($C_1$ and $C_2$), and random values ($\gamma_1$ and $\gamma_2$). The updated position and velocity of a particle are calculated using specific formulas (Eq. G and Eq. H). Over time, the algorithm refines the particles' positions, tracking the global best fitness f($P_g^{best}$), until convergence. The final output of this stage is the position $P_g^{best}$ which maximizes $x_3$, along with the corresponding maximum value of $x_3$.

**Stage 4:** In the final step, the algorithm checks if the best position ($P_g^{best}$) exists in the original dataset. In this process, it finds the data point closest to $P_g^{best}$ and verifies if it matches the computed value within a specified tolerance. If it matches, the result is confirmed as valid. The algorithm then outputs the maximum value of $x_3$ along with its corresponding position, $P_g^{best}$. Flow chart of the proposed algorithm for optimization is given in Fig. 11 and the algorithm is given below.

## 7. Conclusion

In this work, two simple designs of all-optical power splitters (3 dB and 6 dB) have been proposed. The power splitters are designed on a 2D-PC rods-in-air platform where no nonlinear material is used. To obtain the maximum output powers of a 3 dB power divider only 3 junction rods' radii have been optimized whereas in a 6 dB power splitter, the radii of 9 rods (3 rods in each junction) have been optimized. From the FDTD algorithm, it has been realized that all the power splitters are capable of delivering ~99 % of input power to their output ports. Moreover, the response time of 3 dB and 6 dB power dividers have also been measured as 0.4 picoseconds and 0.5 picoseconds respectively. The

optimization of junction rods' radius has been done by applying K-means clustering and Particle Swarm Optimization algorithms. The simple structural design, high efficiency of delivering power to the output ports, absence of optical nonlinearity, and ML-based optimization altogether make the devices capable for future advanced fiber optic networks.

## Consent to participate

N/A.

## Consent for publication

N/A.

## CRediT authorship contribution statement

**Kalyan Kumar Ghosh:** Writing – review & editing, Writing – original draft, Software, Methodology, Investigation. **Haraprasad Mondal:** Writing – review & editing, Writing – original draft, Validation, Supervision, Software, Methodology, Investigation, Formal analysis, Conceptualization. **Himanshu Ranjan Das:** Writing – original draft, Methodology, Formal analysis, Conceptualization. **Mohammad Soroosh:** Writing – original draft, Methodology, Investigation, Formal analysis, Conceptualization. **Sudipta Majumdar:** Validation, Software, Methodology. **Bhargabjyoti Saikia:** Methodology, Investigation, Formal analysis.

## Ethics approval

We affirm that the paper, "Power Optimization of 1:2 and 1:4 Photonic Crystal Based Optical Power Splitters/Combiners Using Machine Learning Algorithms," is unique, has never been published in whole or in part, and is not presently being considered for publication anywhere. Furthermore, we affirm that we have all approved the order of authors indicated in the work.

## Funding

No organization provided funding to the authors for the work they submitted.

## Declaration of competing interest

The authors declare that they have no known competing financial interests or personal relationships that could have appeared to influence the work reported in this paper.

## Acknowledgements

For his gracious assistance and support in carrying out this work, the authors would like to sincerely thank Prof. Mrinal Sen, Associate Professor at the Indian Institute of Technology (ISM), Dhanbad, India.

## Data availability

No data was used for the research described in the article.

## References

Agrawal, G.P., 2010. Fiber-Optic Communication Systems, fourth ed. Wiley.
Ahmed, R., Khan, Md. M., Ahmmed, R., Ahad, A., 2013. Design, simulation & optimization of 2D photonic crystal power splitter. Article ID: 33337 Opt. Photon. 3 (2A), 7. https://doi.org/10.4236/opj.2013.32A002.
Anagha, E.G., Jeyachitra, R.K., 2022. Optimized design of an all-optical XOR gate with high contrast ratio and ultra-compact dimensions. Appl. Phys. B 128, 21. https://doi.org/10.1007/s00340-021-07747-x.
Arunkumar, R., Jayabarathan, J.K., Robinson, S., 2019. Design and analysis of optical Y-splitters based on twodimensional photonic crystal ring resonator. J. Optoelectron. Adv. Mater. 21 (7–8), 435–442.
Assefa, S., Rakich, P.T., Bienstman, P., Johnson, S.G., Petrich, G.S., Joannopoulos, J.D., Kolodziejski, L.A., Ippen, E.P., Smith, H.I., 2004. Guiding 1.5 μm light in photonic crystals based on dielectric rods. Appl. Phys. Lett. 85 (25).
Azar, T.H.A, Alipour-Banaei, H., Zavvari, M., 2018. A high efficiency optical power splitter in a Y-branch photonic crystal for DWDM optical communication systems. Frequenz 72 (1–2), 79–84. https://doi.org/10.1515/freq-2016-0265.
Betsy Saral, T., Robinson, S., Arunkumar, R., 2016. Two-dimensional photonic crystal based compact power splitters. Int. J. Photon. and Opt. Technol. 2 (4), 1–5.
Bienstman, P., Assefa, S., Johnson, S.G., Joannopoulos, J.D., Petrich, G.S., Kolodziejski, L.A., 2003. Taper structures for coupling into photonic crystal slab waveguides. J. Opt. Soc. Am. B 20 (9), 1817–1821.
Danaie, M., Nasirifar, R., Dideban, A., 2017. Design of adjustable Tshaped and Y-shaped photonic crystal power splitters for TM and TE polarizations. Turk. J. Electr. Eng. Comput. Sci. 25 (5), 72. https://doi.org/10.3906/elk-1702-334.
Das, H.R., Mondal, H., 2024. Investigation of plasmonic material-based T-shaped high extinction ratio electro-absorption modulator with different dielectric materials. Optik 313, 171985.
Dutta, H.S., Goyal, A.K., Srivastava, V., Pal, S., 2016. Coupling light in photonic crystal waveguides: a review. Photonics Nanostruct. Fundam. Appl. 20, 41–58.
Farmani, A., Mir, A., Irannejad, M., 2019. 2D-FDTD simulation of ultracompact multifunctional logic gate with nonlinear photonic crystal. J. Opt. Soc. Am. B 36, 811–818.
Fu, Y., Hu, X., Gong, Q., 2013. Silicon photonic crystal all-optical logic gates. Phys. Lett. A 377 (3–4), 329–333.
Jamois, C., Wehrspohn, R.B., Andreani, L.C., Hermann, C., Hess, O., Gosele, U., 2003. Silicon-based twodimensional photonic crystal waveguides. Photon. Nanostruct. 1, 1–13.
Jiang, Y.-C., Liu, S.-B., Zhang, H.-F., Kong, X.-K., 2015. Realization of all-optical half-adder based on self-collimated beams by two-dimensional photonic crystals. Opt. Commun. 348, 90–94.
Jindal, P., Kaur, H.J., 2021. Performance analysis of an ultra- compact power splitter based on 2D photonic crystal in the near IR range for photonic integrated circuits. J. Opt. 50, 395–402. https://doi.org/10.1007/s12596-021-00725-8.
Joannopoulos, J.D., Johnson, S.G., Winn, J.N., Meade, R.D., 2008. Photonic Crystals: Molding the Flow of Light, second ed. Princeton University.
Johnson, S.G., Joannopoulos, J.D., 2001. Block-iterative frequency domain methods for Maxwell's equations in a plane wave basis. Opt. Expr. 8, 173–190.
Karami, P., Yahya, S.I., Chaudhary, M.A., Assaad, M., Roshani, S., Hazzazi, F., Parandin, F., Roshani, S., 2024. Design of a photonic crystal exclusive-OR gate using recurrent neural networks. Symmetry 16, 820. https://doi.org/10.3390/sym16070820.
Karami, P., Mohamadi, A., Parandin, F., 2025. Enhancing integrated optical circuits: optimizing all-optical NAND and NOR gates through deep learning and machine learning. Opt. Quant. Electron. 57, 73. https://doi.org/10.1007/s11082-024-07989-x.
Karami, P., Yahya, S.I., Chaudhary, M.A., Assaad, M., Parandin, F., Roshani, S., Hazzazi, F., Roshani, S., 2025. Design of an optical half-adder based on two-dimensional photonic crystals using feedforward neural networks. Appl. Opt. 64, 973–983.
Keiser, G., 2021. Optical Fiber Communications, fifth ed. McGraw-Hill.
Kok, M., Heesch van, C.M., Geluk, E.J., Sander-Jochem, M.J.H., Tol van der, J.J.G.M., Oei, Y.S., Smit, M.K., 2006. Two dimensional photonic crystals based on InP rods. Proc CNM Research Day, Eindhoven, Conference. CNM Research Day.
Mesri, N., Alipour-Banaei, H., 2017. An optical power divider based on two-dimensional photonic crystal structure. J. Opt. Commun. 38 (2), 129–132. https://doi.org/10.1515/joc-2016-0069.
Mohammadi, M., Mansouri-Birjandi, M.A., 2015. Five-port power splitter based on pillar photonic crystal. IJST, Trans. Electr. Eng. 39, 93–100.
Mondal, H.P., Sen, M., Goswami, K., 2019. Design, and analysis of a 0.9Tb/s 6-channel WDM filter based on photonic crystal waveguides. J. Opt. Soc. Am. B 36 (11), 3181–3188.
Mondal, H.P., Sen, M., Goswami, K., 2019. Design and analysis of all-optical 1-to-2-line decoder based on linear photonic crystal. IET Optoelectron 13 (4), 191–195.
Noori, M., Soroosh, M., Baghban, H., 2017. Self-collimation in photonic crystals: application and opportunities. Ann. Phys. 530, 1700049.
Olsson, B.E., Ohlen, P., Rau, L., Blumenthal, D.J., 2000. A simple and robust 40-Gb/s wavelength converter using fiber cross-phase modulation and optical filtering. IEEE Photon. Technol. Lett. 12, 846–848.
Parandin, F., Kamarian, R., Jomour, M., 2021. A novel design of all-optical half-subtractor using a square lattice photonic crystal. Opt. Quantum Electron. 53, 114. https://doi.org/10.1007/s11082-021-02772-8.
Parandin, F., Karami, P., Mohamadi, A., 2024. Machine learning-driven optimization of photonic crystal structures for superior optical NOR gate performance. Appl. Opt. 63, 6666–6673.
Prakash, C., Sen, M., Mondal, H., Goswami, K., 2018. Design and optimization of a TE pass polarization filter based on a slotted photonic crystal waveguide. J. Opt. Soc. Am. B 35 (8), 1791–1798.
Prather, D.W., Sharkawy, A., Shi, S., Murakowski, J., Schneider, G., 2009. Photonic crystals, theory, applications and fabrication. Wiley Series Pure Appl. Opt.
Rafiee, E., Emami, F., Negahdari, R., 2018. Design of a novel nano plasmonic-dielectric photonic crystal power splitter suitable for photonic integrated circuits. Optik 172, 234–240. https://doi.org/10.1016/j.ijleo.2018.06.006.

Ramaswami, Sivarajan, Sasaki, 2009. Optical Networks: a Practical Perspective, 3rd ed. Morgan Kaufmann.

Runser, R.J., Zhou, D., Coldwell, C., et al., 2001. Interferometric ultrafast SOA-based optical switches: from devices to applications. Opt. Quant. Electron. 33, 841–874. https://doi.org/10.1023/A:1017553819079.

Sakoda, K., 2005. Optical properties of photonic crystals, second ed. Springer Series in Optical Sciences, Germany.

Sen, M., Das, M.K., 2013. Raman mediated all-optical cascadable inverter using silicon-on-insulator waveguides. Opt. Lett. 38, 5192–5195.

Serajmohammadi, S., Alipour-Banaei, H., Mehdizadeh, F., 2015. All optical decoder switch based on photonic crystal ring resonators. Opt. Quant. Electron. 47, 1109–1115. https://doi.org/10.1007/s11082-014-9967-2.

Shih, T.-M., Kurs, A., Dahlem, M., Petrich, G., Soljačić, M., Ippen, E., Kolodziejski, L., Hall, K., Kesler, M., 2008. Super-collimation in photonic crystals composed of silicon rods. Appl. Phys. Lett. 93 (13).

Sohrabi, F., Mahinroosta, T., Hamidi, S.M., 2014. Design of 1×3 power splitter based on photonic crystal ring resonator. Opt. Eng. 53 (11), 115104. https://doi.org/10.1117/1.OE.53.11.115104.

Sukhoivanov, I.A., Guryev, I.V., 2009. Photonic Crystals: Physics and Practical Modeling, first ed. Springer Series in Optical Sciences, Germany.

Tang, C., Dou, X., Lin, Y., Yin, H., Wu, B., Zhao, Q., 2014. Design of all-optical logic gates avoiding external phase shifters in a two-dimensional photonic crystal based on multi-mode interference for BPSK signals. Opt. Commun. 316, 49–55.

Tekeste, M.Y., Yarrison-Rice, J.M., 2006. High efficiency photonic crystal based wavelength demultiplexer. Opt. Express 14, 7931–7942.

Thirumaran, S., Dhanabalan, S.S., Sannasi, I.G., 2021. Design and analysis of photonic crystal ring resonator based 6 × 6 wavelength router for photonic integrated circuits. IET Optoelectron 15, 40–47. https://doi.org/10.1049/ote2.12014.

Tomlinson, W.J., Stolen, R.H., Shank, C.V., 1984. Compression of optical pulses chirped by self-phase modulation in fibers. J. Opt. Soc. Am. B 1, 139–149.

Xavier, S.C., Arunachalam, K., Caroline, E., Johnson, W., 2013. Design of two-dimensional photonic crystal-based all-optical binary adder. Opt. Eng. 52 (2), 025201. https://doi.org/10.1117/1.OE.52.2.025201.

Yablonovitch, E., 1987. Inhibited spontaneous emission in solid-state physics and electronics. Phys. Rev. Lett. 58, 2059–2062.